

## PHYSICAL SCIENCES

## Hypershifted spin spectroscopy with dynamic nuclear polarization at 1.4 K

Zhenfeng Pang<sup>1</sup>, Kirill Sheberstov<sup>1</sup>, Bogdan A. Rodin<sup>1†</sup>, Jake Lumsden<sup>1</sup>, Utsab Banerjee<sup>1‡</sup>, Daniel Abergel<sup>1</sup>, Frédéric Mentink-Vigier<sup>2,3</sup>, Geoffrey Bodenhausen<sup>1</sup>, Kong Ooi Tan<sup>1\*</sup>

Dynamic nuclear polarization (DNP) enhances nuclear magnetic resonance (NMR) sensitivity by transferring polarization from unpaired electrons to nuclei, but nearby nuclear spins are difficult to detect or “hidden” due to strong electron-nuclear couplings that hypershift their NMR resonances. Here, we detect these hypershifted spins in a frozen glycerol-water mixture doped with TEMPOL at ~1.4 K using spin diffusion enhanced saturation transfer (SPIDEST), which indirectly reveals their spectrum. Additionally, we directly observe <sup>1</sup>H NMR lines spanning 10 MHz. The spectrum is confirmed by simulations and density functional theory (DFT) calculations, which verify that the signals originate from intramolecular protons on TEMPOL. Using two-dimensional NMR, we demonstrate polarization transfer from hypershifted to bulk nuclei across a spin diffusion barrier. This methodology provides new insights into the structures of radicals and could aid in designing more efficient DNP polarizing agents. It also complements information on hyperfine interaction accessible by electron paramagnetic resonance (EPR).

## INTRODUCTION

Nuclear magnetic resonance (NMR) is a noninvasive technique that has been widely applied to study materials and biological macromolecules, including catalysts, battery materials, fibrils, and membrane proteins. Nevertheless, the technique suffers from its inherently poor sensitivity. To boost the sensitivity, dynamic nuclear polarization (DNP) (1–3) can be applied to mediate the polarization transfer from unpaired electrons to the nearby nuclear spins that are coupled by electron-nuclear hyperfine interactions. Because of their close proximity (<1 nm) (Fig. 1A) to the unpaired electron, the nearby nuclei experience strong distance- and orientation-dependent hyperfine interactions (Fig. 1B). The polarization of the hyperpolarized nearby nuclear spins is then transferred to more remote bulk nuclear spins via spin diffusion (4, 5). Alternatively, the bulk nuclei can also be polarized directly by the radical if spin diffusion is not substantial due to weak internuclear dipolar couplings as for dilute spins (6).

Although the nearby nuclear spins supposedly play a critical role in mediating polarization transfer by spin diffusion from the unpaired electrons to the bulk nuclear spins, it has been postulated that some of these nearby nuclear spins could not relay the polarization to the bulk if spin diffusion is quenched. Quenching of spin diffusion could be due to a large shift difference, extreme line broadening (Fig. 1B), or rapid relaxation rates that originate from the electron-nuclear hyperfine interactions. Nearby nuclei that do not participate in the spin diffusion process are said to lie within a so-called “spin diffusion barrier” (7–11). Although many attempts have been made to determine the size of the spin diffusion barrier using either theoretical models or indirect experimental observations, the estimates

vary over an order of magnitude (~0.2 to 2 nm) (5, 12–18). It is challenging to observe these nearby spins with excessively broadened or shifted NMR lines, resulting in poor sensitivity below the detection limit and thus the common expression of “invisible” spins (8, 16).

To probe these nearby spins, we have adapted a well-known solution-state NMR experiment known as “chemical exchange saturation transfer” (CEST) (19, 20), which in our context has been re-named “spin diffusion enhanced saturation transfer” (SPIDEST). When applied to paramagnetic samples, SPIDEST shares some similarities with electron-electron double resonance (ELDOR)-detected NMR (EDNMR) (21). We have succeeded in detecting the hidden spins indirectly using SPIDEST and directly via the detection of their free induction decay (FID) (vide infra). Since these spins have now been directly observed, they can no longer be called “hidden”; we shall henceforth refer them as “hypershifted” nuclei and use the symbol <sup>1</sup>H<sub>HS</sub>. The experimental results show that the <sup>1</sup>H spectra of the hypershifted nuclei span a frequency range of ~10 MHz [<sup>1</sup>H shifts of ~35,000 parts per million (ppm) at 6.7 T], which suggests that the hypershifted signals originate from protons that are covalently attached to the nitroxide radicals. The relaxation properties (*T*<sub>1</sub> and *T*<sub>2</sub>) of the hypershifted nuclei <sup>1</sup>H<sub>HS</sub> and the rates of spin diffusion between <sup>1</sup>H<sub>HS</sub> and <sup>1</sup>H<sub>Bulk</sub> were also quantified in this work.

## RESULTS AND DISCUSSION

## Spin diffusion enhanced saturation transfer

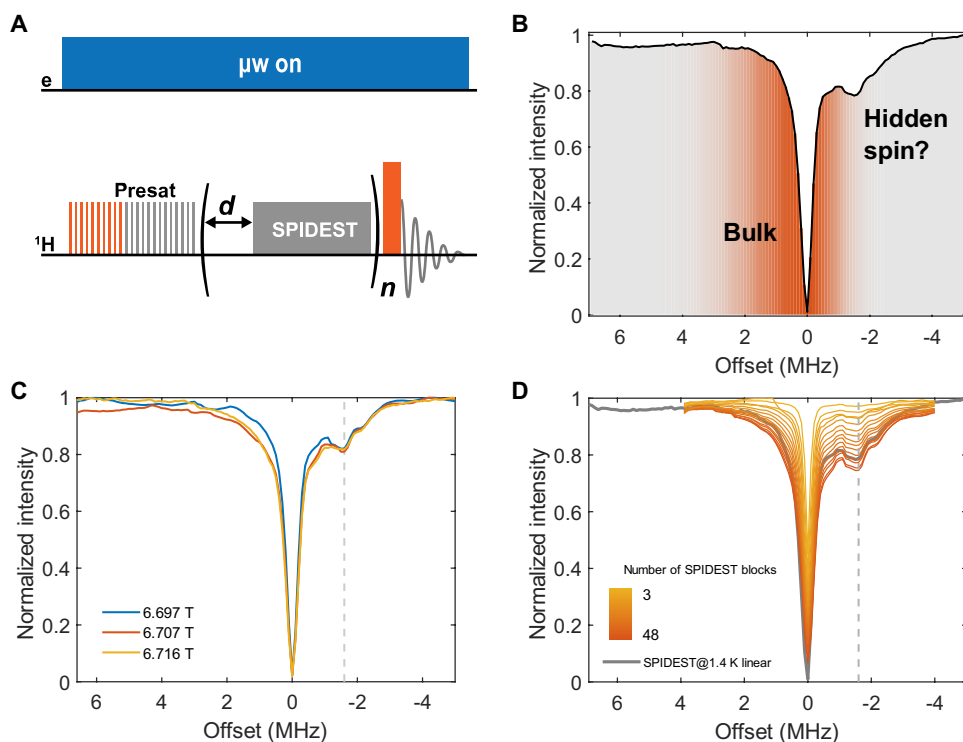
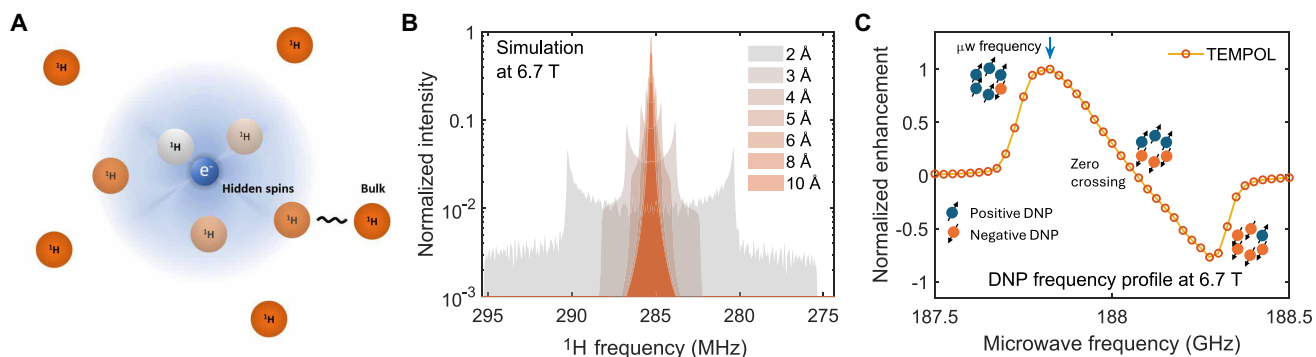
In the SPIDEST experiments, the microwave frequency was set to the positive maximum of the DNP frequency profile (blue arrow in Fig. 1C) and the off-resonance radio frequency (rf) frequencies of the SPIDEST saturation pulses (Fig. 2A) were stepped across a wide range of frequencies where the invisible spins could be resonant, before the direct excitation of the <sup>1</sup>H<sub>Bulk</sub> spins. Note that both the invisible and <sup>1</sup>H<sub>Bulk</sub> spins are hyperpolarized by DNP in our SPIDEST experiments. If the rf frequency of the SPIDEST saturation pulses resonates with the invisible spins that exchange polarization with the bulk spins, the latter will be indirectly saturated, resulting in a decrease of the NMR intensity of the observed <sup>1</sup>H<sub>Bulk</sub> spins. By repeating the experiments using different SPIDEST irradiation frequencies,

<sup>1</sup>Laboratoire des Biomolécules, LBM, Département de Chimie, École Normale Supérieure, PSL University, Sorbonne Université, CNRS, 75005 Paris, France. <sup>2</sup>Department of Chemistry and Biochemistry, Florida State University, Tallahassee, FL 32306, USA. <sup>3</sup>National High Magnetic Field Laboratory, Florida State University, Tallahassee, FL 32310, USA.

\*Corresponding author. Email: kong-ooi.tan@ens.psl.eu

†Present address: NVision Imaging Technologies GmbH, Albert-Einstein-Allee 11, 89081 Ulm, Germany.

‡Present address: Department of Chemistry, TUM School of Natural Sciences, Technical University of Munich, 85748 Garching, Germany.



one obtains a SPIDEST profile (Fig. 2B), which yields a surprising asymmetric shape spanning  $>5$  MHz with a noticeable local minimum at  $-1.6$  MHz. The loss of signal intensity of  $^1\text{H}_{\text{Bulk}}$  following far-off-resonance saturation at  $-1.6$  MHz implies the presence of nuclear spins that interact with  $^1\text{H}_{\text{Bulk}}$  via chemical exchange, nuclear Overhauser effects (NOEs), or spin diffusion. We disregard both

chemical exchange and homonuclear  $^1\text{H}$ - $^1\text{H}$  NOE, as they are unlikely to occur in a frozen solid at 1.4 K (22). We hypothesize that there exists a significant hypershifted proton bath ( $^1\text{H}_{\text{HS}}$ ) that exchanges polarization with  $^1\text{H}_{\text{Bulk}}$  via dipolar-mediated spin diffusion.

To verify the observations and exclude the possibility of rf artifacts, the SPIDEST experiments were repeated with saturation frequencies

chosen in a random order rather than in linear increments. This strategy is commonly used in pulsed ENDOR, where stochastic rf acquisition is used to mitigate artifacts and systematic errors (23). The SPIDEST profile acquired with the stochastic rf scheme is noisier, probably because of temperature fluctuations induced by reflected rf power, which could be significant given that the SPIDEST frequencies can be far ( $\sim$ MHz) from the frequency where the probe is tuned and matched. The two experiments yield similar profiles (fig. S1A) and, hence, confirm that the peak  $-1.6$  MHz is not an artifact. For further verification, we repeated the SPIDEST experiments at slightly different magnetic fields ( $\pm 0.01$  T or  $^1\text{H}$  frequencies  $\pm 0.4$  MHz) by changing the superconducting current in the cryogen-free magnet. The results (Fig. 2C) show that all three local minima coincide at  $-1.6$  MHz, which proves that the frequency depends on the static field, confirming that our observation must be a magnetic resonance effect.

To characterize the spin diffusion from  $^1\text{H}_{\text{HS}}$  to  $^1\text{H}_{\text{Bulk}}$ , the SPIDEST experiments were repeated with different duty cycles of the saturation pulses (by setting the power to zero for part of the pulses in the orange saturation blocks in Fig. 2A). The results (Fig. 2D) clearly show a progressive loss of  $^1\text{H}_{\text{Bulk}}$  signals, uniformly across the entire profile (including both  $^1\text{H}_{\text{Bulk}}$  and the hypershifted peak at  $-1.6$  MHz) as the saturation blocks increase. We did not attempt to fit a buildup curve or to extract a time constant because of the many undetermined parameters (for example, competition between DNP and rf saturation efficiencies,  $T_1$  relaxation of both proton baths, and spin diffusion). Characterizing and quantifying the spin diffusion rates accurately is a challenge beyond the scope of this article. It is, therefore, preferable to observe the hypershifted spins directly (vide infra).

### Direct NMR observation of hypershifted protons $^1\text{H}_{\text{HS}}$

Motivated by the promising results of SPIDEST, we hypothesized that the hypershifted spins resonating near  $-1.6$  MHz in the SPIDEST profile could be observed directly. After the probe was tuned and matched to  $\sim 283.5$  MHz (corresponding to an offset of  $-1.6$  MHz), we successfully observed an NMR peak (Fig. 3A), albeit using a longer excitation pulse than required for exciting the  $^1\text{H}_{\text{Bulk}}$  signal (fig. S2C). To verify that the signals observed are true FID, and not rf ringdown or other artifacts, the experiment was repeated without microwaves. As the signal decreased significantly when the microwave irradiation was turned off (Fig. 3A), it confirms that the signal at  $-1.6$ -MHz offset is a real magnetic resonance and can be DNP enhanced. The DNP enhancement factors of the  $^1\text{H}_{\text{HS}}$  and  $^1\text{H}_{\text{Bulk}}$

resonances were found to be  $\epsilon_{\text{HS}} \sim 43$  and  $\epsilon_{\text{Bulk}} \sim 26$  (fig. S3, C and D), respectively. In addition, we performed echo experiments (fig. S1B) with different  $\tau$  delays. As expected, the echo signals appeared at later times with increasing the value of  $\tau$ . These two control experiments prove that these are real NMR signals hypershifted by about  $-1.6$  MHz from the  $^1\text{H}_{\text{Bulk}}$  Larmor frequency.

From the echo experiments, the transverse echo decay time was determined to be  $T'_{2,\text{HS}} \sim 252$   $\mu\text{s}$  (fig. S1B), which is, unexpectedly, significantly longer than  $T'_{2,\text{Bulk}} \sim 110$   $\mu\text{s}$ . A similar, nonintuitive, effect was also reported in electron decoupling experiments (24, 25). This could be explained as follows: Each bulk proton is coupled to many other bulk protons with a broad range of values of homonuclear dipolar couplings in the  $^1\text{H}$  Zeeman reservoir. On the other hand, the hypershifted protons are dipole coupled to far fewer protons. Hence, the decoherence of the transverse magnetization in echo experiments is faster for the bulk than for the hypershifted protons. In contrast to the bulk protons that suffer from flip-flop terms in the dipolar Hamiltonian, the flip-flop terms that affect the hypershifted protons are partly truncated by the large  $\sim 1.6$ -MHz shift difference. Hence, we reason that the  $2\theta$  pulse applied to  $^1\text{H}_{\text{HS}}$  during the echo experiment is inherently “selective” and decouples the  $^1\text{H}_{\text{HS}}$  spins from the bulk protons, which contributes to longer  $T'_{2,\text{HS}}$ .

To map the entire spectrum of the hypershifted spins, we repeated the experiments with rf carrier frequencies stepped across  $\sim 10$  MHz while keeping the magnetic field  $B_0$  constant. Such an acquisition strategy is a common technique used for observing nuclei with severely broadened lines (often several MHz) by quadrupolar interactions (26). Inspired by solid echo sequences (27), we have also attempted  $\theta$ - $\tau$ - $\theta$ - $\tau$ -echo experiments, but these yield similar results as the  $\theta$ - $\tau$ - $2\theta$ - $\tau$ -echo sequences (fig. S4A). Figure 3B shows that the  $^1\text{H}_{\text{HS}}$  peak intensities are  $\sim 100$  times weaker than the  $^1\text{H}_{\text{Bulk}}$  peaks. The integrated intensity across the entire width of the  $^1\text{H}_{\text{HS}}$  spectrum (skipping the peak due to  $\text{H}_{\text{Bulk}}$ , which is fitted by a single Gaussian function) yields about  $\sim 20\%$  of the total  $^1\text{H}$  signal. Since the DNP enhancement of  $^1\text{H}_{\text{HS}}$  at  $-1.6$  MHz ( $\epsilon_{\text{HS}} \sim 43$ ) is about twice the enhancement of  $^1\text{H}_{\text{Bulk}}$  ( $\epsilon_{\text{Bulk}} \sim 26$ ), this implies that 12% of the  $^1\text{H}$  spins in the DNP sample belong to the  $^1\text{H}_{\text{HS}}$  reservoir. The results are in reasonable agreement with the calculated number of intramolecular protons attached to TEMPOL (8.8%) at a concentration of 60 mM in the DNP juice. This suggests that the hypershifted  $^1\text{H}_{\text{HS}}$  peak is mainly due to intramolecular protons of the radical.

By overlaying the directly observed  $^1\text{H}_{\text{HS}}$  spectrum with the SPIDEST profile, we note that both feature a local extremum at

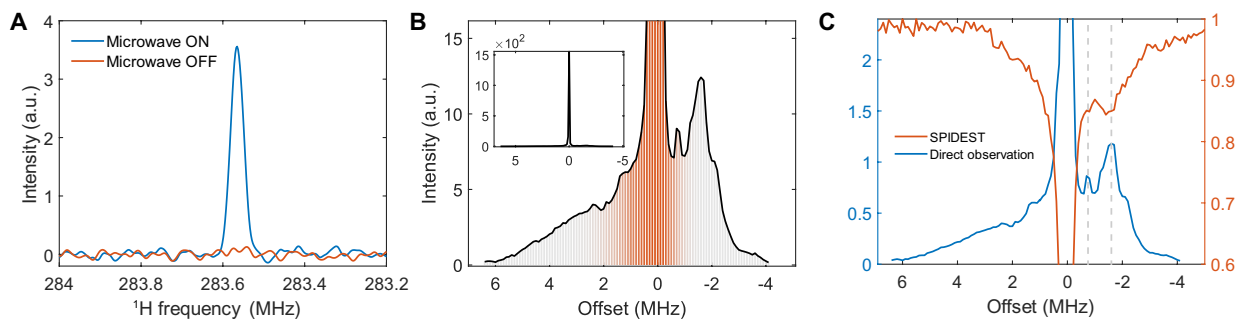


**Fig. 3. Direct experimental observation of  $^1\text{H}_{\text{HS}}$ .** (A)  $^1\text{H}_{\text{HS}}$  signals at an offset of  $-1.6$  MHz acquired with (blue) or without (red) microwave irradiation. (B) Overlay of spectra acquired at different rf offset frequencies. The black envelope shows the outline of all spectra. The inset shows the  $^1\text{H}_{\text{Bulk}}$  peak, which is about 100 $\times$  stronger than the  $^1\text{H}_{\text{HS}}$  signals. (C) Overlaid results from direct observation (blue) and SPIDEST (orange). The vertical dashed lines indicate offsets of  $-1.6$  and  $-0.7$  MHz.

–1.6 MHz with an asymmetric shape (Fig. 3C). The results of these two independent experiments are in good agreement, except that NMR signals were observed in the +3- to +6-MHz region of the directly detected spectrum, but absent in the SPIDEST profile. The results imply that there exists a fraction of the hypershifted protons, particularly those in the +3- to +6-MHz region, do not participate in spin diffusion with  $^1\text{H}_{\text{Bulk}}$ . Presumably, these  $^1\text{H}_{\text{HS}}$  lie within the spin diffusion barrier.

To assign the hypershifted protons, simulations of the  $^1\text{H}$  spectra of the protons attached to the TEMPOL molecule were performed with the Spinach program using literature values of  $^1\text{H}$  hyperfine coupling tensors determined by ENDOR (green plot in Fig. 4A) (28, 29). Note that the simulated  $^1\text{H}_{\text{HS}}$  spectrum reveals an unfamiliar asymmetric Pake pattern due to the high electron polarization at 6.7 T and 1.4 K. Only one-half of the Pake pattern can be observed if only the state of lowest energy is populated, assuming that the electron relaxation time  $T_{1e}$  is long enough (30). Simulated  $^1\text{H}$  spectra of an isolated two-spin system (one electron and one proton) at both 1.4 and 80 K are shown in Fig. 4B, demonstrating that the asymmetry disappears with lower electron polarization. We have attempted to measure the  $^1\text{H}_{\text{HS}}$  spectrum at a slightly higher temperature of 4.2 K, but the sensitivity was  $\sim 30$  times lower than at 1.4 K, potentially due to insufficient microwave power to yield efficient DNP and faster relaxation rates of  $^1\text{H}_{\text{HS}}$  at higher temperatures.

As the simulated  $^1\text{H}_{\text{HS}}$  spectrum (Fig. 4A) shows an excellent fit to the peak at –1.6 MHz, we can confidently assert that the –1.6-MHz

peak originates from the intramolecular protons on the nitroxide radical. Despite a satisfactory agreement between the simulated and experimental data, the simulated results could not reproduce the long trailing edge in the range between +3 and +6 MHz observed in the experiments. This could be due to the solvent protons close to the nitroxide. To examine the contribution of the solvent protons to the  $^1\text{H}_{\text{HS}}$  spectrum, we repeated the experiment on the hydrophobic TEMPO dissolved in a fully deuterated solvent mixture composed of benzene- $d_6$  and toluene- $d_8$ . The standard DNP juice cannot be used because the imperfect chemical purity and deuteration of commercial glycerol- $d_8$  yields a nonnegligible  $^1\text{H}$  background signal (25). The  $^1\text{H}$  spectrum of TEMPO in the 3- to 6-MHz range is partly suppressed compared to the TEMPOL spectrum. Moreover, an anomalous peak at –0.7 MHz (marked with #) is present in both TEMPOL and TEMPO spectra but absent in the calculated ENDOR spectra. We hypothesize that the signal at –0.7 MHz arises from the proton attached to C4 (Fig. 4A) that was not reported in the ENDOR literature. Our hypothesis is supported by the experimental results obtained on TEMPONE, which lacks a proton attached to C4 (fig. S4C). To determine the origin of the  $^1\text{H}$  signals that are responsible for the long trailing edge and unambiguously assign the peak at –0.7 MHz, density functional theory (DFT) calculations were performed on TEMPOL. The simulated  $^1\text{H}_{\text{HS}}$  spectrum based on DFT matches with the experimental data quite well, including both the 3- to 6-MHz range and the peak at –0.7 MHz. Further analysis shows that the long trailing edge could be due to the methyl protons (fig. S4E), which

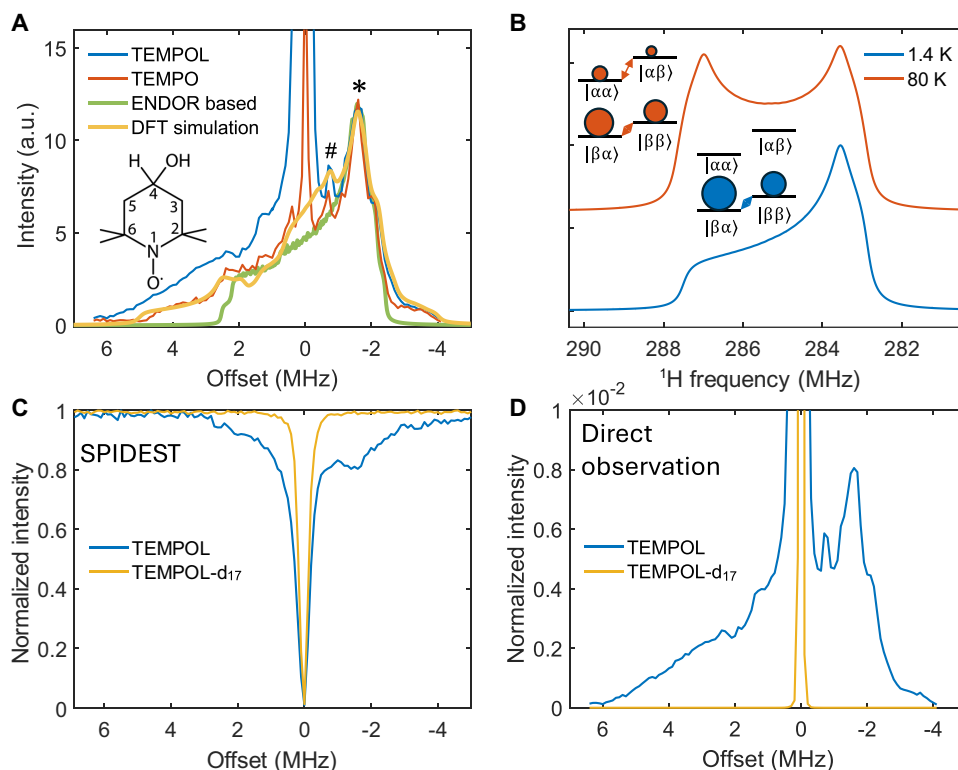


**Fig. 4. Assignment of  $^1\text{H}_{\text{HS}}$ .** (A) Comparison of experimental  $^1\text{H}$  spectrum of TEMPOL (blue) with simulated spectra using hyperfine tensor values from ENDOR (green) (28) and DFT simulations (yellow). An experimental  $^1\text{H}$  spectrum of TEMPO (red) is also shown here. The  $^1\text{H}_{\text{HS}}$  peaks at –1.6 MHz of all spectra are normalized to the same intensity. (B) Simulated  $^1\text{H}$  spectrum of an electron-proton pair with a near-unity electron polarization at a sample temperature  $T = 1.4$  K (blue) that is asymmetric, in contrast to the typical symmetric Pake pattern expected at 80 K (orange) (66). (C) SPIDEST of protonated and deuterated TEMPOL in DNP juice. (D) Directly observed spectra of protonated and deuterated TEMPOL in DNP juice. The y axis is scaled down by  $\sim 100\times$  with respect to the normalized  $^1\text{H}_{\text{Bulk}}$  peak.

were also reported in the literature (31). Moreover, the  $-0.7$ -MHz signal could arise from the protons attached to C4.

As a control experiment, we repeated the experiments on TEMPOL-d<sub>17</sub> to confidently assign the  $^1\text{H}_{\text{HS}}$  signal to  $^1\text{H}$  attached to the nitroxides. Note that there is no significant change in DNP performance observed between the protonated TEMPOL and deuterated TEMPOL-d<sub>17</sub> samples, in agreement with a previous study (32). Both the SPIDEST profile (Fig. 4C) and the direct NMR observation experiments (Fig. 4D) yield a significantly narrower peak with a full width at half maximum (FWHM) of  $\leq 400$  kHz. The disappearance of the broad lines observed on TEMPOL-d<sub>17</sub> again proves that the broad  $^1\text{H}_{\text{HS}}$  signal originates mostly from protons attached to the nitroxide, while the narrow peak could originate from solvent protons in the vicinity of the radical.

### Spin diffusion between bulk and hypershifted protons

Although the SPIDEST experiments (Fig. 2B) show a polarization loss of  $^1\text{H}_{\text{Bulk}}$  upon rf irradiation to saturate the  $^1\text{H}_{\text{HS}}$  protons, this does not necessarily prove that the decreased  $^1\text{H}_{\text{Bulk}}$  polarization was transferred to  $^1\text{H}_{\text{HS}}$ . To prove this point, a two-dimensional (2D) exchange spectroscopy (EXSY) sequence [also known as nuclear Overhauser effect spectroscopy (NOESY)] (Fig. 5A) was used to probe  $^1\text{H}_{\text{Bulk}}$ - $^1\text{H}_{\text{HS}}$  correlation. The pulse sequence can be used to probe a transfer of longitudinal magnetization due to spin diffusion. As it is impossible to excite the entire 10-MHz-wide spectrum of  $^1\text{H}_{\text{HS}}$  with a limited rf amplitude, the 2D EXSY sequence was modified by setting the first two pulses on-resonance with  $^1\text{H}_{\text{Bulk}}$  at

0 MHz, while the third pulse was set to excite the strongest  $^1\text{H}_{\text{HS}}$  peak at  $-1.6$  MHz. For detection, the probe was tuned and matched to  $-0.8$  MHz, halfway between the two peaks. For optimal sensitivity, the frequencies of the first two pulses and the third pulse were chosen to match the two most intense peaks. This strategy is reminiscent of double electron resonance (DEER) (33) for the measurement of dipolar couplings between two electrons.

Figure 5B shows a cross peak, which provides direct evidence that the polarization was transferred from  $^1\text{H}_{\text{Bulk}}$  to  $^1\text{H}_{\text{HS}}$ . Besides, we observed an unexpected diagonal peak ( $F_1 = F_2 = 0$ ) in the 2D spectrum. Although the offset of  $\sim 1.6$  MHz between the third rf pulse and  $^1\text{H}_{\text{Bulk}}$  is too large to allow efficient excitation, only 1% excitation of the strong  $^1\text{H}_{\text{Bulk}}$  peak (Fig. 3B) is needed to yield a diagonal peak with a similar intensity as the cross peak. To confirm this hypothesis, we replaced the third pulse by a two-pulse echo detection, which should refocus  $^1\text{H}_{\text{HS}}$  but suppresses  $^1\text{H}_{\text{Bulk}}$ . The diagonal peak was suppressed (fig. S5). Despite this, we prefer to use a single excitation pulse (Fig. 5A) before detection due to its higher sensitivity.

To measure the polarization buildup mediated by spin diffusion, we recorded multiple 1D EXSY experiments with varying mixing times. The delay between the first two pulses was fixed to  $t_1 = 0.6$   $\mu\text{s}$ , all other parameters being the same as for the 2D experiment. Although the diagonal peak intensity decreases as expected when the mixing time increases, we observed that the cross peak intensity has a sign opposite to the diagonal peak (Fig. 5, C and D) for mixing times  $\tau_m < 0.5$  s and goes through zero before reaching a plateau

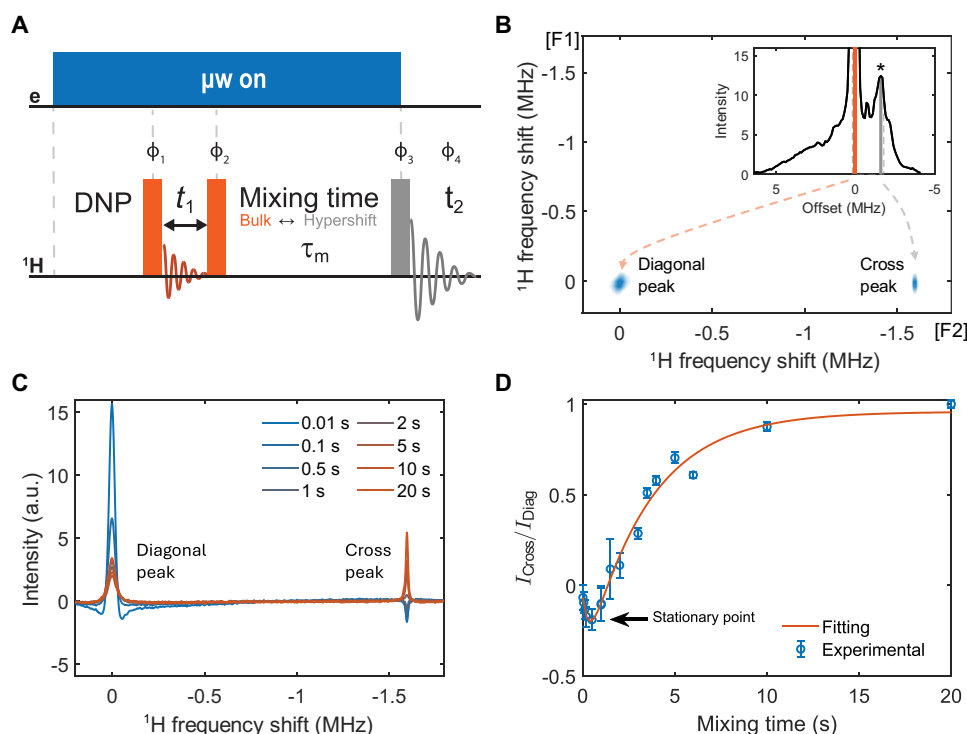


**Fig. 5. Probing polarization transfer from  $^1\text{H}_{\text{Bulk}}$  to  $^1\text{H}_{\text{HS}}$  using 2D NMR.** (A) 2D EXSY sequence where the first two pulses (10  $\mu\text{s}$  @ 30 W, orange) are centered at the  $^1\text{H}_{\text{Bulk}}$  frequency, while the third (95  $\mu\text{s}$  @ 30 W, gray) pulse is centered at an offset of  $-1.6$  MHz. (B) 2D NMR spectrum with a cross peak between  $^1\text{H}_{\text{Bulk}}$  (at  $F_1 = 0$ ) and  $^1\text{H}_{\text{HS}}$  (at  $F_2 = -1.6$  MHz). The inset shows the 1D spectrum of Fig. 3B. (C) Superposition of 1D spectra with mixing times  $\tau_m$  ranging from 10 ms to 20 s. (D) Normalized cross peak intensities ( $I_{\text{Cross}}/I_{\text{Diag}}$ ) as a function of the mixing time, showing how the sign of the cross peaks changes. A bi-exponential fit (red) yields time constants  $T^{\text{short}} = 0.33$  s and  $T^{\text{long}} = 3.3$  s.

after  $\tau_m \sim 10$  s. This may be explained by first realizing that the spin environments around the nitroxides, which have different orientations with respect to the  $B_0$  field (microscopic view), might not benefit from the same DNP conditions as the ensemble average of all spins across the sample (macroscopic view). For instance, although the NMR spectrum recorded at the DNP zero-crossing position ( $\sim 188$  GHz in Fig. 1C) yields an apparent zero DNP enhancement, this does not mean that there is no DNP. Instead, on a microscopic level, there are equal numbers of positive- and negative-polarized  $^1\text{H}$  spins, which yield a net zero DNP enhancement on the observable  $^1\text{H}_{\text{Bulk}}$ . Hence, at the positive DNP condition for the bulk ( $\sim 187.8$  GHz), there may still be a number of nitroxides with orientations that satisfy the negative DNP condition, and hence negatively polarize their surrounding  $^1\text{H}_{\text{HS}}$  spins (although the bulk signal is positive). This helps explain our observation that the  $^1\text{H}_{\text{HS}}$  signal at  $-1.6$  MHz is initially negatively polarized (for mixing times  $\tau_m < 10$  ms) and becomes more negatively polarized ( $\tau_m \sim 500$  ms) due to spin diffusion from nearby negatively polarized  $^1\text{H}_{\text{HS}}$ . As the mixing time  $\tau_m$  increases, the positive polarization from the dominant  $^1\text{H}_{\text{Bulk}}$  (or other positively polarized  $^1\text{H}_{\text{HS}}$ ) starts to diffuse toward  $^1\text{H}_{\text{HS}}$ . This insight on the orientation dependence of  $^1\text{H}_{\text{HS}}$  (see the Supplementary Materials for a detailed discussion) is inaccessible in conventional DNP-enhanced NMR spectroscopy that detects only  $^1\text{H}_{\text{Bulk}}$ .

Unlike conventional 2D NMR experiments, where the recovery delay is usually chosen to be at least  $1.27 \times T_1$  for optimal sensitivity, such a scheme is not practical for these experiments because of the long DNP buildup time ( $\geq 15$  min) and poor  $^1\text{H}_{\text{HS}}$  sensitivity. Instead, many dummy scans before the 2D experiment (see the “Spin diffusion enhanced saturation transfer” section) were used so that the polarization reaches a transient equilibrium, and a shorter preparation time ( $\sim 6$  s) was sufficient for a 2D experiment within a reasonable time scale ( $\sim 1$  day versus  $\sim 5$  months). Nevertheless, the total polarization increases as the mixing time  $\tau_m$  increases (Fig. 5A), which indicates that some undesirable DNP builds up during the mixing time. This yields an unreliable characterization of the spin diffusion rate. Hence, the ratio of cross peak to the diagonal peak intensities ( $I_{\text{Cross}}/I_{\text{Diag}}$ ) against the mixing time  $\tau_m$  was plotted (Fig. 5D) for a fair comparison. A bi-exponential fit yields a fast spin diffusion rate  $k^{\text{fast}} \sim 3 \text{ s}^{-1}$  that characterizes the initial negative polarization surge, and a larger but slower component  $k^{\text{slow}} \sim 0.3 \text{ s}^{-1}$  that governs the delayed buildup of the positive polarization.

Clearly, the EXSY spectra show a significant polarization transfer between  $^1\text{H}_{\text{HS}}$  and  $^1\text{H}_{\text{Bulk}}$  despite their frequency separation ( $\sim 1.6$  MHz) that is significantly larger than the homonuclear  $^1\text{H}$ - $^1\text{H}$  dipolar couplings in a partially deuterated sample—a surprising observation that appears to contradict standard NMR predictions. We believe that the experimental observation could be rationalized by a series of spin diffusion processes involving many intermediate protons  $^1\text{H}_{\text{HS}}$  with offset frequencies between 0 and  $\sim -1.6$  MHz. A detailed investigation of the polarization-transfer pathway is beyond the scope of this work but is planned in future studies. For instance, this can be investigated by mapping the polarization across the entire  $^1\text{H}_{\text{Bulk}}$ - $^1\text{H}_{\text{HS}}$  network, which can be achieved by varying the frequency of the third pulse in the 2D experiment (Fig. 5A). Nevertheless, such experiments would be impractically long, unless pulsed DNP could be used to accelerate the DNP buildup rates and boost the enhancement factors (34, 35). On the other hand, we intend to apply the same methodology to investigate narrow-line radicals like 1,3-bisdiphenylene-2-phenylallyl (BDPA) or trityls that

yield simpler DNP frequency profiles to improve the understanding of polarization-transfer pathways in DNP.

In recent literature, some theoretical studies and models have been applied to address the roles of electrons in the nuclear spin diffusion process (36–38). Besides electrons, it is also known that  $^1\text{H}_{\text{Bulk}}$  participate in cross-talk with deuterons of the solvent (32, 39, 40), which could also relay the polarization to  $^1\text{H}_{\text{HS}}$ . A similar phenomenon was reported for hyperfine-coupled  $^{13}\text{C}$  spins in diamonds, which relay their polarization to the bulk  $^{13}\text{C}$  spins, although the  $^{13}\text{C}$ - $^{13}\text{C}$  couplings are 100 times weaker than the hyperfine couplings (11).

We also re-investigated the resurgence of hyperpolarization (HypRes) reported by Stern *et al.* (16), who showed that the  $^1\text{H}_{\text{Bulk}}$  polarization recovers at some delays after rf saturation of the same  $^1\text{H}_{\text{Bulk}}$  nuclei. It was shown that nuclear spin hyperpolarization was transferred from hidden  $^1\text{H}$  spins (or hypershifted  $^1\text{H}_{\text{HS}}$  spins in our nomenclature) to the  $^1\text{H}_{\text{Bulk}}$  bath [see figure 3 of Stern *et al.* (16)]. To verify their predictions, we repeated their experiments (Fig. 6A) but observing  $^1\text{H}_{\text{HS}}$  at  $-1.6$  MHz directly instead of  $^1\text{H}_{\text{Bulk}}$ . An accelerated loss of  $^1\text{H}_{\text{HS}}$  polarization (Fig. 6B) was observed when the  $^1\text{H}_{\text{Bulk}}$  spins are saturated after DNP, confirming, once again, the existence of spin diffusion between  $^1\text{H}_{\text{HS}}$  and  $^1\text{H}_{\text{Bulk}}$ . The time evolution of the difference spectrum (i.e., with and without saturation) was fitted with a biexponential function, yielding two time constants  $T^{\text{short}} = 30.7$  s and  $T^{\text{long}} = 1023$  s. We believe that the faster process is dominated by  $T_{1,\text{HS}}$  and spin diffusion, while the slower process is governed by  $T_{1,\text{Bulk}}$  and thermal mixing via the  $^2\text{H}$  reservoir in the perdeuterated DNP juice (32).

We have directly observed nuclear spins close to an unpaired electron that were previously believed to be unobservable and hence known as hidden spins. The observations were carried out on nitroxide-doped samples using a homebuilt 6.7-T DNP NMR spectrometer operating at 1.4 K. The previously hidden nuclei, now renamed hypershifted nuclei, are observed in a wide  $^1\text{H}$  spectrum spanning no less than 10 MHz, which matches the size of the intramolecular hyperfine interactions between the  $^1\text{H}$  spins and the unpaired electron of TEMPOL. Despite the large observed shifts, the results of the SPIDEST- or CEST-like experiments show that the spin diffusion rates between the hypershifted protons  $^1\text{H}_{\text{HS}}$  and the bulk protons  $^1\text{H}_{\text{Bulk}}$  are far from negligible. EXSY-like 2D exchange experiments were carried out to quantify the spin diffusion rates across the so-called spin diffusion barrier. Collectively, we refer to our methodology and the set of experiments performed in this work (including SPIDEST, EXSY, or 2D EXSY and direct observation of wide lines) as hypershifted spin spectroscopy. Our methodology has allowed us to quantify relaxation rates and spin diffusion rates of the hypershifted spins, parameters that can contribute to a deeper understanding of DNP mechanisms. For example, one could improve the rationalization of cross-talk phenomena between spin reservoirs reported in a recent study (32). Additionally, a better characterization of the nuclear spins surrounding the radicals could help design better polarizing agents for DNP (41–43). Besides fundamental studies, our methodology could be applied in standard dissolution DNP or electron paramagnetic resonance (EPR) spectrometers equipped with NMR detection capabilities to study a wide variety of paramagnetic systems (especially those containing lanthanide ions) including catalysts, luminescent materials, semiconductors, and battery materials (6, 44–46). Besides, we have shown that hypershifted spin spectroscopy can provide complementary and sometimes

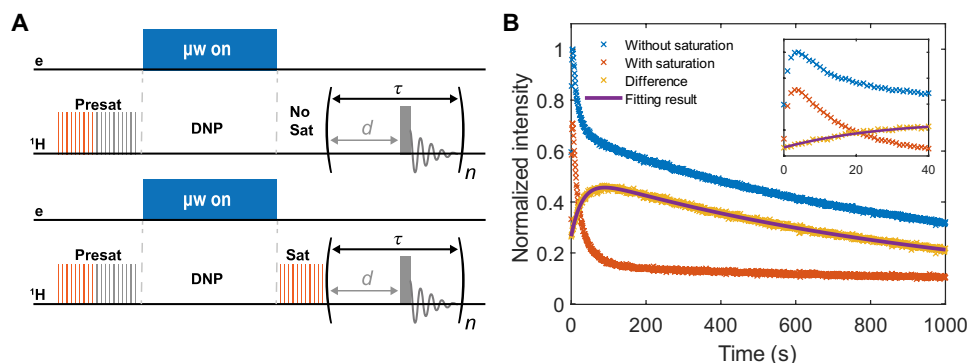


**Fig. 6. Depolarization of  $^1\text{H}_{\text{HS}}$  by saturation transfer to  $^1\text{H}_{\text{Bulk}}$ .** (A) Pulse sequences for observation on  $^1\text{H}_{\text{HS}}$  with saturation of  $^1\text{H}_{\text{Bulk}}$  (bottom) or without saturation (top). The orange and gray pulses have rf frequencies centered on the  $^1\text{H}_{\text{Bulk}}$  and  $^1\text{H}_{\text{HS}}$  signals, respectively, like in Fig. 5A. (B) Results for the experiments without (blue)/with (red) saturation of  $^1\text{H}_{\text{Bulk}}$  and their difference (yellow). The difference curve (yellow) was fitted with a bi-exponential function (purple). A surge of  $^1\text{H}_{\text{HS}}$  was observed a few seconds after the microwaves were switched off (inset). This could be due to a new equilibrium when microwave-dependent relaxation rates are altered, a phenomenon reported recently in literature (67). The initial surges cancel each other in the difference between the two curves.

new information that is not easily accessible using conventional pulsed EPR ENDOR experiments. The latter were performed on single crystals instead of the doped glassy glycerol-water mixtures used in modern DNP experiments. Moreover, our technique is performed at higher magnetic fields than most conventional pulsed EPR experiments (47–49), thus providing better resolution. In conclusion, we believe that the methodology developed here could provide information that is complementary to ENDOR experiments, but without needing to detect any EPR signals.

## MATERIALS AND METHODS

### Sample preparation and NMR experiments

Both TEMPOL and  $d_{17}$ -TEMPOL (CAS: 100326-46-3, 97% D, Sigma-Aldrich) were dissolved in DNP juice ( $d_8$ -glycerol/ $\text{D}_2\text{O}/\text{H}_2\text{O}$  in a 6:3:1 ratio by volume), while the hydrophobic TEMPO was dissolved in a mixture of  $d_6$ -benzene (99.5%  $^2\text{H}$ ) and  $d_8$ -toluene (99.5%  $^2\text{H}$ ) with a 1:1 volume ratio. The concentrations of TEMPOL and TEMPO in all samples were 60 mM. About 200  $\mu\text{l}$  was pipetted into a 5-mm NMR tube cut to a length of 1.5 cm.

In most DNP experiments, 64 pre-saturation blocks interleaved with delays of 2 s were applied to fully saturate the polarizations of both  $^1\text{H}_{\text{Bulk}}$  and  $^1\text{H}_{\text{HS}}$  before switching on the microwaves. Each block consists of 128 pulses (10  $\mu\text{s}$  with 30 W) separated by 1-ms intervals (fig. S3A). Note that it is important to increase the number of saturation block until the NMR signals reach equilibrium to obtain a reliable SPIDEEST profile. For the SPIDEEST experiment, 48 SPIDEEST blocks (similar to the pre-saturation block except that only 10 W of rf power was used to minimize rf reflection and heating) using  $\sim 130$ -ms pulses alternating with 1-s delays were applied before signal acquisition (Fig. 2A). The rf offset of the SPIDEEST pulses was increased from  $-5$  to  $+6.9$  MHz in 0.1-MHz steps. The probe remained tuned and matched to the resonance frequency of the  $^1\text{H}_{\text{Bulk}}$  spins throughout the experiments. To measure the DNP buildup curves of  $^1\text{H}_{\text{Bulk}}$  (fig. S3B), the same pre-saturation blocks as used for SPIDEEST were applied before NMR acquisition. The nutation profiles of the  $^1\text{H}_{\text{Bulk}}$  and  $^1\text{H}_{\text{HS}}$  spins are distinctly different from typical sinusoidal curves (fig. S2C). We believe that the strong  $^1\text{H}$  dipolar coupling network that competes with the weak  $B_1$  field is responsible for this behavior. Since it was challenging to accurately

determine the  $B_1$  field strength and  $90^\circ$  pulse length, we used the pulse durations that yield the maximum signal, i.e., 10  $\mu\text{s}$  at 30 W for exciting  $^1\text{H}_{\text{Bulk}}$  and 95  $\mu\text{s}$  at 30 W for  $^1\text{H}_{\text{HS}}$ , respectively. To observe the hypershifted spins directly (Fig. 3B), microwave irradiation was applied until the DNP polarization reached a plateau, and a  $\theta$ - $\tau$ - $2\theta$ - $\tau$ -echo sequence was applied with durations of 10 and 20  $\mu\text{s}$  for the  $\theta$  and  $2\theta$  pulses, respectively, with 30-W rf power and a delay  $\tau = 45$   $\mu\text{s}$ . Eight scans with inter-scan delays of 1 s were accumulated for each frequency.

To measure spin diffusion between  $^1\text{H}_{\text{Bulk}}$  and  $^1\text{H}_{\text{HS}}$ , we adopted 2D EXSY (Fig. 5A) (50), except that the rf frequency of the third pulse differs from the first two pulses. The detection frequency was set in the middle between the resonance frequencies of  $^1\text{H}_{\text{Bulk}}$  and  $^1\text{H}_{\text{HS}}$ . Because of the implementation of multiple rf frequencies (or rotating frames) in this adapted 2D experiment, it is important to pre-calculate the phase of the second pulse according to the evolution time  $t_1$  and the offset frequency so that the detection scheme in the indirect dimension is properly used (51). A sequence of 384 dummy scans was applied to ensure that a steady state and a stable temperature were reached before acquisition. The pulse sequence (TopSpin 3.5 pl 7) and 2D data are available on Zenodo (<https://zenodo.org/records/12735275>).

### DNP spectrometer with cryogen-free magnet

All experiments were performed on a cryogen-free (also known as “dry”) magnet (Cryogenic Ltd., reference J4112) (Fig. 7). The assembly is similar to the older 9.4-T cryogen-free magnet in our laboratory (52), except that the new cryo-free magnet uses a 1.5-W pulse tube (PT) cryocooler (SRP-182B2S) with an F100H (Sumitomo) compressor, and an integrated variable temperature insert (iVTI) with an inner diameter of 50 mm to accommodate an NMR probe. The iVTI can reach a temperature of  $\sim 1.4$  K when it is continuously pumped at  $\sim 0.4$  mbar during a closed-loop operation using an ECODRY 40 plus Leybold pump. The manufacturer specified a  $B_0$  field inhomogeneity of  $\leq 30$  ppm over a cylindrical volume of 25 mm diameter and 25 mm height. However, we measured a field homogeneity of  $\sim 4$  ppm across a 5-mm NMR tube containing deuterated water of  $\sim 1$  cm height at room temperature.

In closed-loop operation, the helium gas is cycled through a 50-liter external helium storage tank, an external charcoal trap immersed in

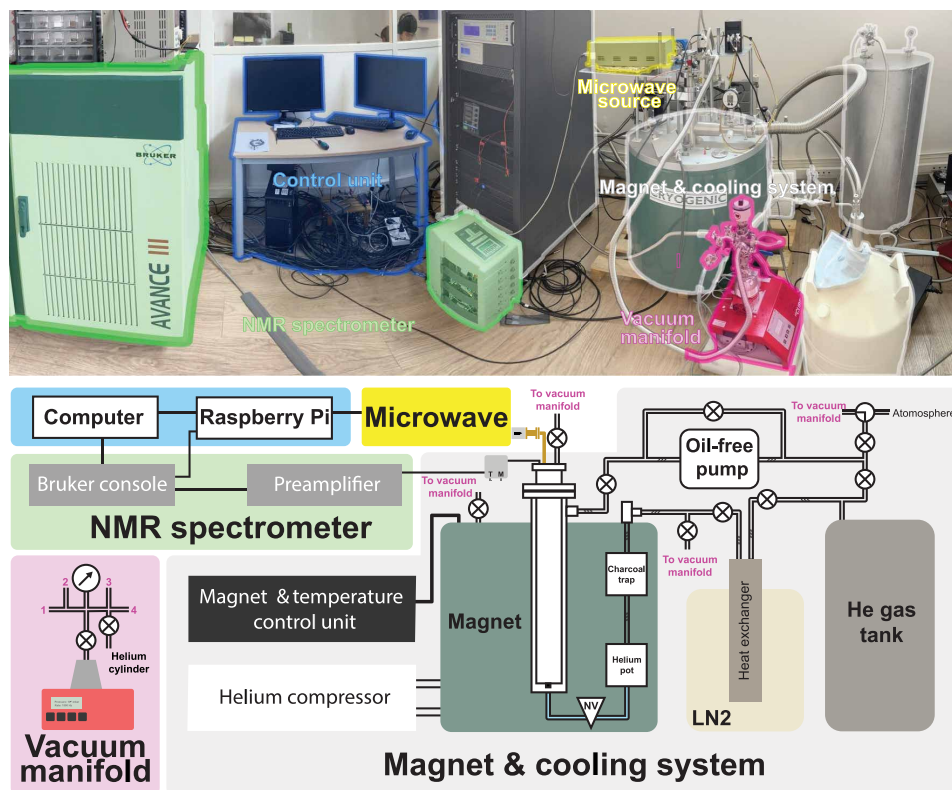


**Fig. 7. Schematic diagram of the homebuilt DNP-NMR spectrometer.** The system consists of a cryogen-free magnet with a helium recirculation system (white), a microwave source (yellow), an NMR console (green), a control unit (blue), and a vacuum manifold on top of a pump (purple).

liquid nitrogen at 77 K, an internal charcoal trap, a 200-ml helium pot, and the iVTI. The last three are built-in features of the magnet system. The helium flow rate and the pressure in the iVTI can be controlled by an automated needle valve, which is composed of an ethanol-filled cell that controls the valve position by thermal contraction/expansion via a computer-controlled heater. Nevertheless, we manually controlled the needle valve for most experiments. The iVTI temperature fluctuates  $\pm 0.01$  K over 24 hours, which is sufficiently stable for our experiments. Although the magnet can be ramped to 9.4 T, we chose to operate at 6.7 T because our 188-GHz microwave source can provide more power ( $\sim 150$  mW) than our 263-GHz source ( $\sim 60$  mW). The magnet is interfaced with a Bruker AVANCE III console equipped with a 100-W BLAH100 E amplifier.

### DNP probe and microwave source

A custom-built probe was used for the experiments. It has a similar design as other DNP systems in our laboratory, except for the homemade rf coil and waveguide (52). This probe is equipped with a ruthenium oxide (RuO) temperature sensor (range: 30 mK to 305 K, Lake Shore Cryotronics Inc.) and two coaxial cables with stainless steel outer conductors (UT-085B-SS) to minimize heat transfer. To improve the sensitivity and the  $B_1$  homogeneity, a horizontal solenoidal coil perpendicular to the static  $B_0$  field was used instead of a saddle coil. The five-turn solenoid was connected in series with a 0.6-pF capacitor (fig. S6B) and remotely tuned using an external tuning and matching box. With broad-range variable capacitors (10 to 100 pF, Sprague-Goodman), the probe can be tuned over a range of  $\sim 20$  MHz ( $285 \pm 10$  MHz). The copper cavity in the probe is

sealed following the same procedure as described in a previous work (52), i.e., red-colored silicone (CAF 1 from Bluestar Silicones) was applied and then pumped to  $\sim 1$  mbar while immersed in liquid nitrogen at 77 K. This is a crucial step as a bad seal will lead to contamination of the helium gas, which leads to unstable temperatures or ice blockages of the system. In the latter case, a complete warm-up of the system may be necessary, a process that can take 2 to 3 days. To stabilize the temperature and minimize rf arcing, we filled the sample space in the probe with room-temperature helium gas after it was inserted into the iVTI. The pressure of the helium gas in the closed cavity is  $\sim 3$  mbar at 1.4 K (53, 54).

The microwaves are generated by an IMPATT diode (model VCOM-05, ELVA-1, Tallinn, Estonia) with an output power of 150 mW over a 1-GHz tuning range ( $188 \pm 0.5$  GHz). About  $\sim 1$ -mW microwave power was measured at the sample position using a power meter (Ophir Optronics, model 3A-P-THz) at room temperature. The significant power loss between the source and sample is attributed to the lossy stainless-steel waveguide and the homebuilt microwave bend. Although the microwave source is equipped for both amplitude and frequency modulation over a range of 100 MHz with a repetition rate of 5 kHz, these functions were not yet used in our experiments. The microwave source is interfaced with the NMR console via a Raspberry Pi 4b (fig. S7).

### DFT calculations

The input structures for DFT were generated using Avogadro v2.0 (55–57), optimized using ORCA v5.0.4 and the functional r2SCAN-3c method (58–62). For TEMPOL, a polarizable continuum model

water (63) was used to mimic the dielectric properties of the glycerol/water mixture. From the optimized structures, the hyperfine couplings were calculated using PBE0 and EPR-III basis sets (64, 65). The output of the DFT calculations is shown in the Supplementary Materials.

## Supplementary Materials

### The PDF file includes:

Supplementary Text  
Figs. S1 to S10  
Tables S1 to S3  
Legend for data S1  
References

### Other Supplementary Material for this manuscript includes the following:

Data S1

## REFERENCES AND NOTES

- A. Abragam, M. Goldman, Principles of dynamic nuclear polarisation. *Rep. Prog. Phys.* **41**, 395–467 (1978).
- T. Wenckebach, *Essentials of Dynamic Nuclear Polarization* (Spindrift Publications, 2016).
- A. S. L. Thankamony, J. J. Wittmann, M. Kaushik, B. Corzilius, Dynamic nuclear polarization for sensitivity enhancement in modern solid-state NMR. *Prog. Nucl. Magn. Reson. Spectrosc.* **102–103**, 120–195 (2017).
- N. Bloembergen, On the interaction of nuclear spins in a crystalline lattice. *Physica* **15**, 386–426 (1949).
- N. A. Prisco, A. C. Pinon, L. Emsley, B. F. Chmelka, Scaling analyses for hyperpolarization transfer across a spin-diffusion barrier and into bulk solid media. *Phys. Chem. Chem. Phys.* **23**, 1006–1020 (2021).
- D. Jardón-Álvarez, M. Leskes, Metal ions based dynamic nuclear polarization: MI-DNP. *Prog. Nucl. Magn. Reson. Spectrosc.* **138–139**, 70–104 (2023).
- J. P. Wolfe, R. S. Markiewicz, Near-nuclei magnetic resonance of  $\text{CaF}_2:\text{Yb}^{3+}$ . *Phys. Rev. Lett.* **30**, 1105–1107 (1973).
- J. P. Wolfe, NMR of nuclei near rare-earth ions in yttrium ethyl sulfate. *Phys. Rev. B* **16**, 128–145 (1977).
- J. P. Wolfe, Direct observation of a nuclear spin diffusion barrier. *Phys. Rev. Lett.* **31**, 907–910 (1973).
- A. R. King, J. P. Wolfe, R. L. Ballard, NMR of nuclei near a paramagnetic impurity in crystals. *Phys. Rev. Lett.* **28**, 1099–1102 (1972).
- D. Pagliero, P. R. Zangara, J. Henshaw, A. Joy, R. H. Acosta, J. A. Reimer, A. Pines, C. A. Meriles, Optically pumped spin polarization as a probe of many-body thermalization. *Sci. Adv.* **6**, eaaz6986 (2020).
- Y. Hovav, A. Feintuch, S. Vega, Theoretical aspects of dynamic nuclear polarization in the solid state – The solid effect. *J. Magn. Reson.* **207**, 176–189 (2010).
- A. A. Smith, B. Corzilius, O. Haze, T. M. Swager, R. G. Griffin, Observation of strongly forbidden solid effect dynamic nuclear polarization transitions via electron-electron double resonance detected NMR. *J. Chem. Phys.* **139**, 214201 (2013).
- K. O. Tan, M. Mardini, C. Yang, J. H. Ardenkjær-Larsen, R. G. Griffin, Three-spin solid effect and the spin diffusion barrier in amorphous solids. *Sci. Adv.* **5**, eaax2743 (2019).
- S. K. Jain, C.-J. Yu, C. B. Wilson, T. Tabassum, D. E. Freedman, S. Han, Dynamic nuclear polarization with vanadium(IV) metal centers. *Chem* **7**, 421–435 (2021).
- Q. Stern, S. F. Cousin, F. Mentink-Vigier, A. C. Pinon, S. J. Elliott, O. Cala, S. Jannin, Direct observation of hyperpolarization breaking through the spin diffusion barrier. *Sci. Adv.* **7**, eabf5735 (2021).
- A. Chessari, S. F. Cousin, S. Jannin, Q. Stern, Role of electron polarization in nuclear spin diffusion. *Phys. Rev. B* **107**, 224429 (2023).
- C. Ramanathan, Dynamic nuclear polarization and spin diffusion in nonconducting solids. *Appl. Magn. Reson.* **34**, 409–421 (2008).
- P. C. M. Van Zijl, N. N. Yadav, Chemical exchange saturation transfer (CEST): What is in a name and what isn't? *Magn. Reson. Med.* **65**, 927–948 (2011).
- M. J. Jaroszewicz, A. R. Altenhof, R. W. Schurko, L. Frydman, Sensitivity enhancement by progressive saturation of the proton reservoir: A solid-state NMR analogue of chemical exchange saturation transfer. *J. Am. Chem. Soc.* **143**, 19778–19784 (2021).
- P. Schosseler, T. Wacker, A. Schweiger, Pulsed ELDOR detected NMR. *Chem. Phys. Lett.* **224**, 319–324 (1994).
- X. Ji, T. V. Can, F. Mentink-Vigier, A. Bornet, J. Milani, B. Vuichoud, M. A. Caporini, R. G. Griffin, S. Jannin, M. Goldman, G. Bodenhausen, Overhauser effects in non-conducting solids at 1.2 K. *J. Magn. Reson.* **286**, 138–142 (2018).
- B. Epel, D. Arieli, D. Baute, D. Goldfarb, Improving W-band pulsed ENDOR sensitivity - random acquisition and pulsed special TRIPLE. *J. Magn. Reson.* **164**, 78–83 (2003).
- N. Alaniva, E. P. Saliba, E. L. Sesti, P. T. Judge, A. B. Barnes, Electron decoupling with chirped microwave pulses for rapid signal acquisition and electron saturation recovery. *Angew. Chem. Int. Ed. Engl.* **58**, 7259–7262 (2019).
- K. O. Tan, L. Yang, M. Mardini, C. B. Cheong, B. Driesschaert, M. Dincă, R. G. Griffin, Observing nearby nuclei on paramagnetic trityls and MOFs via DNP and electron decoupling. *Chem. Eur. J.* **28**, e202202556 (2022).
- D. Massiot, I. Farnan, N. Gautier, D. Trumeau, A. Trokner, J. P. Coutures,  $^{71}\text{Ga}$  and  $^{69}\text{Ga}$  nuclear magnetic resonance study of  $\beta\text{-Ga}_2\text{O}_3$ : Resolution of four- and six-fold coordinated Ga sites in static conditions. *Solid State Nucl. Magn. Reson.* **4**, 241–248 (1995).
- J. Jeener, P. Broekaert, Nuclear magnetic resonance in solids: Thermodynamic effects of a pair of rf pulses. *Phys. Rev.* **157**, 232–240 (1967).
- M. Brustolon, A. L. Maniero, M. F. Ottaviani, M. Romanelli, U. Segre, Proton hyperfine tensors in nitroxide radicals. *J. Phys. Chem.* **94**, 6589–6594 (1990).
- H. J. Hogben, M. Krzystyniak, G. T. P. Charnock, P. J. Hore, I. Kuprov, Spinach - A software library for simulation of spin dynamics in large spin systems. *J. Magn. Reson.* **208**, 179–194 (2011).
- A. Bornet, A. Pinon, A. Jhajharia, M. Baudin, X. Ji, L. Emsley, G. Bodenhausen, J. H. Ardenkjær-Larsen, S. Jannin, Microwave-gated dynamic nuclear polarization. *Phys. Chem. Chem. Phys.* **18**, 30530–30535 (2016).
- D. Ondercin, T. Sandreczki, R. W. Kreilick, Low temperature NMR studies of polycrystalline nitroxide radicals. *J. Magn. Reson.* **34**, 151–169 (1979).
- B. A. Rodin, V. Thalakkottor, M. Baudin, N. Birilirikis, G. Bodenhausen, A. V. Yurkovskaya, D. Abergel, Quantitative analysis of cross-talk in partly deuterated samples of nuclear spins hyperpolarized by dynamic nuclear polarization (DNP) in the thermal mixing regime. *Phys. Chem. Chem. Phys.* **25**, 15040–15051 (2023).
- O. Schiemann, C. A. Heubach, D. Abdullin, K. Ackermann, M. Azarkh, E. G. Bagryanskaya, M. Drescher, B. Endeward, J. H. Freed, L. Galazzo, D. Goldfarb, T. Hett, L. Esteban Hofer, L. Fábregas Ibáñez, E. J. Hustedt, S. Kucher, I. Kuprov, J. E. Lovett, A. Meyer, S. Ruthstein, S. Saxena, S. Stoll, C. R. Timmel, M. Di Valentin, H. S. McHaourab, T. F. Prisner, B. E. Bode, E. Bordinon, M. Bennati, G. Jeschke, Benchmark test and guidelines for DEER/PELDOR experiments on nitroxide-labeled biomolecules. *J. Am. Chem. Soc.* **143**, 17875–17890 (2021).
- K. O. Tan, S. Jawla, R. J. Temkin, R. G. Griffin, "Pulsed dynamic nuclear polarization" in *Handbook of High Field Dynamic Nuclear Polarization*, B. Corzilius, R. G. Griffin, S. Vega, V. K. Michaelis, Eds. (John Wiley & Sons, 2019), pp. 339–352.
- K. O. Tan, R. T. Weber, T. Van Can, R. G. Griffin, Adiabatic solid effect. *J. Phys. Chem. Lett.* **11**, 3416–3421 (2020).
- G. von Witte, S. Kozerke, M. Ernst, Two-electron two-nucleus effective Hamiltonian and the spin diffusion barrier. arXiv:2407.10319 [physics.chem-ph] (2024).
- N. Wilj, J. H. Ardenkjær-Larsen, G. Jeschke, Reverse dynamic nuclear polarisation for indirect detection of nuclear spins close to unpaired electrons. *Magn. Reson.* **3**, 161–168 (2022).
- J. J. Wittmann, M. Eckardt, W. Harneit, B. Corzilius, Electron-driven spin diffusion supports crossing the diffusion barrier in MAS DNP. *Phys. Chem. Chem. Phys.* **20**, 11418–11429 (2018).
- I. Kaminker, D. Shimon, Y. Hovav, A. Feintuch, S. Vega, Heteronuclear DNP of protons and deuterons with TEMPOL. *Phys. Chem. Chem. Phys.* **18**, 11017–11041 (2016).
- D. Shimon, Y. Hovav, I. Kaminker, A. Feintuch, D. Goldfarb, S. Vega, Simultaneous DNP enhancements of  $^1\text{H}$  and  $^{13}\text{C}$  nuclei: Theory and experiments. *Phys. Chem. Chem. Phys.* **17**, 11868–11883 (2015).
- A. Venkatesh, G. Casano, Y. Rao, F. De Biasi, F. A. Perras, D. J. Kubicki, D. Siri, S. Abel, H. Karoui, M. Yulikov, O. Ouari, L. Emsley, Deuterated TEKPol Biradicals and the spin-diffusion barrier in MAS DNP. *Angew. Chem. Int. Ed. Engl.* **62**, e202304844 (2023).
- F. A. Perras, M. Pruski, Large-scale *ab initio* simulations of MAS DNP enhancements using a Monte Carlo optimization strategy. *J. Chem. Phys.* **149**, 154202 (2018).
- S. Chatterjee, A. Venkatesh, S. T. Sigurdsson, F. Mentink-Vigier, Role of protons in and around strongly coupled nitroxide biradicals for cross-effect dynamic nuclear polarization. *J. Phys. Chem. Lett.* **15**, 2160–2168 (2024).
- W. Li, Q. Zhang, J. J. Joos, P. F. Smet, J. S. A. Der Günne, Blind spheres of paramagnetic dopants in solid state NMR. *Phys. Chem. Chem. Phys.* **21**, 10185–10194 (2019).
- I. B. Moroz, M. Leskes, Dynamic nuclear polarization solid-state NMR spectroscopy for materials research. *Annu. Rev. Mater. Res.* **52**, 25–55 (2022).
- D. Jardón-Álvarez, T. Malka, J. van Tol, Y. Feldman, R. Carmieli, M. Leskes, Monitoring electron spin fluctuations with paramagnetic relaxation enhancement. *J. Magn. Reson.* **336**, 107143 (2022).
- A. Meyer, S. Dechert, S. Dey, C. Höbartner, M. Bennati, Measurement of angstrom to nanometer molecular distances with  $^{19}\text{F}$  nuclear spins by EPR/ENDOR spectroscopy. *Angew. Chem. Int. Ed. Engl.* **132**, 381–387 (2020).
- J. R. Harmer, "Hyperfine spectroscopy—ENDOR" in *EPR Spectroscopy: Fundamentals and Methods*, D. Goldfarb, S. Stoll, Eds. (John Wiley & Sons, 2016), pp. 1493–1514.

49. D. A. Erilov, R. Bartucci, R. Guzzi, A. A. Shubin, A. G. Maryasov, D. Marsh, S. A. Dzuba, L. Sportelli, Water concentration profiles in membranes measured by ESEEM of spin-labeled lipids. *J. Phys. Chem. B* **109**, 12003–12013 (2005).
50. J. Jeener, B. H. Meier, P. Bachmann, R. R. Ernst, Investigation of exchange processes by two-dimensional NMR spectroscopy. *J. Chem. Phys.* **71**, 4546–4553 (1979).
51. K. F. Sheberstov, E. Sistaré Guardiola, D. Jeannerat, Everything you wanted to know about phase and reference frequency in one- and two-dimensional NMR spectroscopy. *Magn. Reson. Chem.* **58**, 376–389 (2020).
52. M. Baudin, B. Vuichoud, A. Bornet, G. Bodenhausen, S. Jannin, A cryogen-consumption-free system for dynamic nuclear polarization at 9.4 T. *J. Magn. Reson.* **294**, 115–121 (2018).
53. V. D. Arp, R. D. Mccarty, “Thermophysical properties of helium-4 from 0.8 to 1500 K with pressures to 2000 MPa” (NIST Technical Note 1334, 1989).
54. F. Pobell, *Matter and Methods at Low Temperatures* (Springer Berlin Heidelberg, 2007).
55. W. A. de Jong, A. M. Walker, M. D. Hanwell, From data to analysis: Linking NWChem and Avogadro with the syntax and semantics of Chemical Markup Language. *J. Cheminform.* **5**, 25 (2013).
56. M. D. Hanwell, W. A. de Jong, C. J. Harris, Open chemistry: RESTful web APIs, JSON, NWChem and the modern web application. *J. Cheminform.* **9**, 55 (2017).
57. M. D. Hanwell, D. E. Curtis, D. C. Lonie, T. Vandermeersch, E. Zurek, G. R. Hutchison, Avogadro: An advanced semantic chemical editor, visualization, and analysis platform. *J. Cheminform.* **4**, 17 (2012).
58. F. Neese, The ORCA program system. *WIREs Comput. Mol. Sci.* **2**, 73–78 (2012).
59. S. Grimme, A. Hansen, S. Ehlert, J.-M. Mewes, r2SCAN-3c: A “Swiss army knife” composite electronic-structure method. *J. Chem. Phys.* **154**, 064103 (2021).
60. F. Neese, Software update: The ORCA program system—Version 5.0. *WIREs Comput. Mol. Sci.* **12**, (2022).
61. F. Neese, F. Wennmohs, U. Becker, C. Ripplinger, The ORCA quantum chemistry program package. *J. Chem. Phys.* **152**, 224108 (2020).
62. S. Lehtola, C. Steigemann, M. J. T. Oliveira, M. A. L. Marques, Recent developments in libxc—A comprehensive library of functionals for density functional theory. *SoftwareX* **7**, 1–5 (2018).
63. A. V. Marenich, C. J. Cramer, D. G. Truhlar, Universal solvation model based on solute electron density and on a continuum model of the solvent defined by the bulk dielectric constant and atomic surface tensions. *J. Phys. Chem. B* **113**, 6378–6396 (2009).
64. D. P. Chong, *Recent Advances in Density Functional Methods* (World Scientific, 1995), vol. 1 of *Recent Advances in Computational Chemistry*.
65. C. Adamo, V. Barone, Toward reliable density functional methods without adjustable parameters: The PBE0 model. *J. Chem. Phys.* **110**, 6158–6170 (1999).
66. B. Aghelnejad, S. Marhabaie, M. Baudin, G. Bodenhausen, D. Carnevale, Spin thermometry: A straightforward measure of Millikelvin deuterium spin temperatures achieved by dynamic nuclear polarization. *J. Phys. Chem. Lett.* **11**, 3219–3225 (2020).
67. G. von Witte, A. Himmler, S. Kozerke, M. Ernst, Relaxation enhancement by microwave irradiation may limit dynamic nuclear polarization. *Phys. Chem. Chem. Phys.* **26**, 9578–9585 (2024).
68. F. Ohzeki, L. D. Kispert, C. Arroyo, M. Steffan, Electron nuclear double resonance study of the spin-label tanol (tempol) oriented in the inclusion compound 2'-hydroxy-2,4,4,7,4'-pentamethylflavan. *J. Phys. Chem.* **86**, 4011–4016 (1982).
69. D. Guarin, D. Carnevale, M. Baudin, P. Pelupessy, D. Abergel, G. Bodenhausen, Effects of microwave gating on nuclear spin echoes in dynamic nuclear polarization. *J. Phys. Chem. Lett.* **13**, 175–182 (2022).

**Acknowledgments:** We thank M. Baudin and E. Kryukov (Cryogenics Ltd.) for providing support for the installation and maintenance of the cryogenic-free magnet. We are grateful to J. Korvink (Karlsruhe Institute of Technology) for providing a Bruker AVANCE III console.

**Funding:** This work was supported by funding obtained from the French National Research Agency: PulsedDNP (ANR-20-ERC9-0008) and HFPulsedDNP (ANR-21-CE29-0019). G.B. and K.S. acknowledge funding from the European Research Council for the ERC Synergy grant “Highly Informative Drug Screening by Overcoming NMR Restrictions” (HISCORE, grant agreement number 951459). The National High Magnetic Field Laboratory (NHMFL) is funded by the National Science Foundation division of Materials Research (DMR-2128556) and the State of Florida. **Author contributions:** K.O.T. and Z.P. designed the research. Z.P. performed the experiments. Z.P., K.S., F.M.-V., and K.O.T. analyzed the data. B.A.R. and D.A. performed preliminary experiments. Z.P., J.L., U.B., and K.O.T. assembled and contributed to the maintenance of the equipment. F.M.-V. performed the DFT calculations. G.B. and K.O.T. acquired fundings required for the instruments and research, respectively. All authors contributed to writing the paper. **Competing interests:** The authors declare that they have no competing interests. **Data and materials availability:** All data needed to evaluate the conclusions in the paper are present in the paper and/or the Supplementary Materials. More results of SPIDEST and direct observation (fig. S1), simulations of hyperfine-coupled  $^1\text{H}$  NMR spectra, nutation profiles of  $^1\text{H}_{\text{Bulk}}$  and  $^1\text{H}_{\text{HS}}$  (fig. S2), DNP buildup curves and enhancements of  $^1\text{H}_{\text{Bulk}}$  and  $^1\text{H}_{\text{HS}}$  (fig. S3), directly observed patterns acquired by different echo sequences and their simulations (fig. S4), 2D spin diffusion NMR with an echo detection (fig. S5), images of the DNP probes (fig. S6), the interface between the NMR spectrometer and the microwave source (fig. S7), and  $T_{1\rho}$  measurements of  $^1\text{H}_{\text{Bulk}}$  (fig. S8). Results of the DFT calculations of nitroxide radicals. The raw NMR data and TOPSPIN pulse program of SPIDEST and 2D EXSY are available in <https://zenodo.org/records/12735275>. A summary of the author-reviewer interactions during the peer review process is included in the “Review Interaction Summary.”

Submitted 14 July 2024  
Accepted 4 November 2024  
Published 11 December 2024  
10.1126/sciadv.adr7160